

The merger remnant NGC 3610 and its globular cluster system: a large-scale study

Lilia P. Bassino^{1,2★} and Juan P. Caso^{1,2★}

¹Facultad de Ciencias Astronómicas y Geofísicas de la Universidad Nacional de La Plata, and Instituto de Astrofísica de La Plata (CCT La Plata – CONICET, UNLP), Paseo del Bosque S/N, B1900FWA La Plata, Argentina

²Consejo Nacional de Investigaciones Científicas y Técnicas, Rivadavia 1917, C1033AAJ Ciudad Autónoma de Buenos Aires, Argentina

Accepted 2016 December 28. Received 2016 December 28; in original form 2016 October 21

ABSTRACT

We present a photometric study of the prototype merger remnant NGC 3610 and its globular cluster (GC) system, based on new Gemini/GMOS and Advanced Camera for Surveys/*Hubble Space Telescope* archival images. Thanks to the large field of view of our GMOS data, larger than previous studies, we are able to detect a ‘classical’ bimodal GC colour distribution, corresponding to metal-poor and metal-rich GCs, at intermediate radii and a small subsample of likely young clusters of intermediate colours, mainly located in the outskirts. The extent of the whole GC system is settled as about 40 kpc. The GC population is quite poor, about 500 ± 110 members that corresponds to a low total specific frequency $S_N \sim 0.8$. The effective radii of a cluster sample are determined, including those of two spectroscopically confirmed young and metal-rich clusters, that are in the limit between GC and UCD sizes and brightness. The large-scale galaxy surface-brightness profile can be decomposed as an inner embedded disc and an outer spheroid, determining for both larger extents than earlier research (10 and 30 kpc, respectively). We detect boxy isophotes, expected in merger remnants, and show a wealth of fine-structure in the surface-brightness distribution with unprecedented detail, coincident with the outer spheroid. The lack of symmetry in the galaxy colour map adds a new piece of evidence to the recent merger scenario of NGC 3610.

Key words: galaxies: elliptical and lenticular, cD – galaxies: evolution – galaxies: individual: NGC 3610 – galaxies: star clusters: general.

1 INTRODUCTION

Globular cluster systems (GCSs) have been extensively studied in the past two decades, but a great effort has been focused mainly in early-type galaxies in dense environments. The large number of globular clusters (GCs) present in these systems (e.g. Dirsch et al. 2003; Bassino et al. 2006; Harris, Harris & Alessi 2013, and references therein) favours the statistical study of GCs, but restricts our knowledge to these particularly evolved systems. Despite early-type galaxies in low environments usually have rather poor GCSs (e.g. Spitler et al. 2008; Caso et al. 2013b; Lane, Salinas & Richtler 2013), their characteristics might provide clues to figure out the evolutionary history of the galaxy itself (e.g. Caso, Bassino & Gómez 2015; Escudero et al. 2015; Salinas et al. 2015).

NGC 3610 is considered as a prototype of an intermediate-age merger remnant (Howell et al. 2004), classified as peculiar lenticular or shell elliptical galaxy (e.g. de Vaucouleurs et al. 1991, and NED, NASA/IPAC Extragalactic Database). The presence of a

‘fine-structure’ of shells, plumes, boxy isophotes, and ‘X-features’ is widely considered as typical of disc–disc mergers of similar mass galaxies (e.g. Barnes & Hernquist 1992; Hernquist & Spergel 1992). Located in a low-density environment, NGC 3610 is included in the group LGG 234 (García 1993) or the NGC 3642 group (Fouque et al. 1992), in both cases a five-member group composed of the same galaxies. In fact, Madore, Freedman & Bothun (2004) identified four physical companions (with known redshifts) within 300 kpc and $\pm 225 \text{ km s}^{-1}$ from the central galaxy.

The complex structure of NGC 3610 has been studied for decades. In their analysis of about 160 early-type galaxies, Ebneter, Davis & Djorgovski (1988) had already detected that NGC 3610 possess boxy isophotes. The structure of NGC 3610 has originally been studied by Scorza & Bender (1990), who pointed out at the unusual presence of an inner disc in an elliptical galaxy, while Schweizer & Seitzer (1992) selected this galaxy as the one presenting the richest fine-structure among their sample of 69 E and S0 merger candidates. Michard & Marchal (1994) studied the morphology of over 100 E–S0 galaxies and pointed that NGC 3610 has a strongly twisted and peculiar envelope as well as an asymmetric structure, presenting an embedded inner disc. Later on, Whitmore et al. (1997)

* E-mail: lbassino@fcaglp.unlp.edu.ar (LPB); jpcaso@fcaglp.unlp.edu.ar (JPC)

performed a complementary study of the galaxy and its GCS based on *Hubble Space Telescope* (*HST*) data, presenting evidence that it is a dynamically young elliptical.

Whitmore et al. (1997) also pointed to the existence of an intermediate age population of GCs in NGC 3610, that might have originated in a past event related to the peculiar structure of this galaxy. Afterwards, the inner GCS was studied by Whitmore et al. (2002) and Goudfrooij et al. (2007) on the basis of images obtained with the Wide Field Planetary Camera 2 and the Advanced Camera for Surveys (ACS), respectively, both on board the *HST*. They revealed an unusual behaviour of the red metal-rich GC luminosity function (GCLF), being this subpopulation of intermediate age ($\sim 1.5\text{--}4$ Gyr) and formed during a gas-rich merger. The inner half of such subpopulation (for radii smaller than ~ 45 arcsec) showed a flattening in the GCLF that is consistent with the predictions of GC disruption models (e.g. Fall & Zhang 2001). Thus, it is a likely consequence of the stronger tidal field in the inner regions that cause a more effective low-mass cluster disruption than further out. Alternatively, the outer half (up to a galactocentric distance ~ 100 arcsec) is consistent with a power-law GCLF (see also Goudfrooij et al. 2004).

In addition, a small sample of GCs has been spectroscopically confirmed (Strader, Brodie & Huchra 2003; Strader, Brodie & Forbes 2004), including a couple of young and metal-rich ones. They are identified as W6 and W11, with ages of 1–2 Gyr and 1–3 Gyr old, and metallicities $[Z/H] = +0.4$ and $+0.7$, respectively. These ages are in agreement with the estimate of 1.6 ± 0.5 Gyr obtained for NGC 3610 by Denicoló et al. (2005). According to such result, it is inferred that the intermediate-age clusters formed in the disc–disc merger that has probably originated the galaxy. Later on, Georgiev, Goudfrooij & Puzia (2012) obtained photometric ages and metallicities for a sample of 50 bright GC candidates (some of them already studied by Strader et al. 2003, 2004), using optical and near-IR imaging. By means of colour–colour diagrams based on that photometric combination, it is possible to break the age–metallicity degeneracy. Comparing with the spectroscopically derived parameters, the metallicities are in agreement while photometric ages are ~ 2 Gyr older than spectroscopic ones, though the age difference becomes smaller for more metal-rich GCs. The age and metallicity distributions obtained by Georgiev et al. (2012) also point to their bright cluster sample being dominated by a metal-rich and intermediate-age subpopulation.

This paper has been planned as a complement to the previous ones, as our observational data will allow us to cover one of the largest field of view (FOV) used to study this galaxy and its GCS so far. Thus, we will be able to establish the whole GCS extension, perform a homogeneous comparison of the GC colour distributions in different radial regimes, as well as analyse the outer regions of the surface-brightness distribution of the galaxy itself.

The most recent distance determinations for NGC 3610, based on surface-brightness fluctuations (SBF) gives ~ 35 Mpc (Cantiello et al. 2007; Tully et al. 2013), remarkably larger than previous ones (Blakeslee et al. 2001; Tonry et al. 2001). Its heliocentric radial velocity is 1707 ± 5 km s $^{-1}$ (Cappellari et al. 2011), lower than expected for the redshift-independent distances. In the following, we will adopt the recent SBF estimates, hence a distance modulus $m - M = 32.7 \pm 0.1$.

This paper is organized as follows. The observations and data reduction are presented in Section 2, the results are described in Section 3 and Section 4 is devoted to the discussion. Finally, a summary and the concluding remarks are given in Section 5.

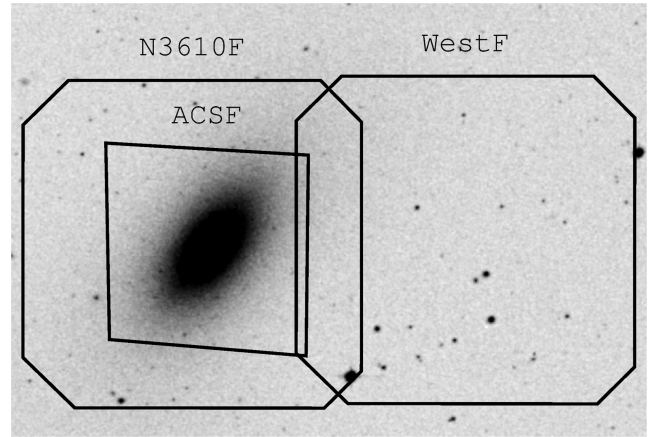


Figure 1. Two GMOS-S fields from our programme, and the smaller ACSF field obtained from the *HST* Data Archive, superimposed on an *R* image from the Palomar Observatory Sky Survey. The image size is 11 arcmin \times 7.5 arcmin. North is up, east to the left.

2 OBSERVATIONS AND REDUCTION

2.1 Observational data

The data set consists of images obtained with GMOS (Gemini North) in g' , r' and i' filters, during semester 2013A (programme GN2013A-Q-42, PI: J.P. Caso), plus ACS (*HST*) images in $F555W$ and $F814W$ filters (programme 9409, PI: P. Goudfrooij) obtained from the *HST* Archive, and originally observed during 2003 June.

The GMOS images correspond to two slightly overlapped fields (Fig. 1), one of them centred on the galaxy NGC 3610, and the other one located to the west (hereafter ‘N3610F’ and ‘WestF’, respectively). The point-sources located in the overlapping region will allow any possible zero-point differences in the corresponding magnitudes to be determined. The exposure times were 4×450 s in g' , 4×210 s in r' and 4×270 s in i' . Each set of exposures was slightly dithered, in order to fill in the gaps of the GMOS field and to efficiently remove cosmic rays and bad pixels.

The ACS field (ACSF) is also centred on NGC 3610 (see Fig. 1). The exposure times were 6410 s in filter $F555W$ (two 2330 s observations plus a 1770 s third one) and 6060 s in filter $F814W$ (two 2330 s observations plus a 1770 s third one). The processed images were downloaded from the *HST* Data Archive. IRAF tasks GEOMAP and GEOTRAN were used to register these images, due to differences in the position of their FOV. Additionally, another ACS field of the 47 Tuc outskirts was used to model the point spread function (PSF). These observations were carried out in the same filters as the NGC 3610 images, during 2003 June (programme 9656), being the exposure time of 30 s.

2.2 Photometry and point-source selection

First, the surface-brightness profile of NGC 3610 was obtained with the ELLIPSE and the corresponding synthetic galaxy, generated with BMODEL (both IRAF tasks), was subtracted from the original image in order to improve the detection of point-sources as much as possible.

For the GMOS fields, the software SExtractor (Bertin & Arnouts 1996) was applied to the i' image, which was selected because it has the higher signal-to-noise ratio (S/N), in order to obtain an initial point-source catalogue. As the effective radii (R_{eff}) of classical GCs is usually smaller than 10 pc (e.g. Brüns & Kroupa 2012),

at the adopted distance the NGC 3610 GCs are seen as point-sources on our images. Then, we used the `SEXTRACTOR` parameter `CLASS_STAR` to eliminate the extended sources from our catalogue. The photometry was performed with the `DAOPHOT` package (Stetson 1987) within `IRAF`. A second-order variable PSF was generated for each filter, employing a sample of bright stars, well distributed over the field. The final point-source selection was made with the χ and sharp parameters, from the task `ALLSTAR`.

In the case of ACS data, GC-like objects might be marginally resolved at the distance of NGC 3610 (e.g. Caso et al. 2013a, 2014). Hence, we applied `SEXTRACTOR` to images in both filters, but considered as likely GC candidates those sources with elongation smaller than 2 and full width at half-maximum (FWHM) smaller than 5 pixel. Similar criteria have already been used for identifying GCs on ACS images (e.g. Jordán et al. 2004, 2007). Approximately 40 to 50 relatively isolated bright stars from the 47 Tuc images were used to obtain the PSF for each filter. Then, aperture photometry was performed on the NGC 3610 field, with an aperture radius of 5 pixel, which is almost three times the FWHM obtained for the foreground stars. The software `ISHAPE` (Larsen 1999) was used to calculate structural parameters for the GC candidates, considering a typical R_{eff} of 0.35 pixel (see Section 3.5). Approximately 16 GC and ultra-compact dwarf (UCD) candidates brighter than $F814W = 23$ mag, relatively isolated and with $0.3 < R_{\text{eff}} < 0.4$ pixel in both filters were used to calculate aperture corrections, resulting in -0.07 mag for $F555W$ and -0.12 mag for $F814W$.

2.3 Photometric calibration and background estimation

A field of standard stars from the list of Smith & et al. (2002) was observed for our GMOS programme, during the same nights than the field N3610F. We obtained the growth curve, and hence aperture corrections, from the standard stars' aperture photometry for several aperture radii. Then, we fit transformation equations of the form:

$$m_{\text{std}} = ZP + m_{\text{inst}} - K_{\text{MK}} \times (X - 1),$$

where m_{std} and m_{inst} are the standard and instrumental magnitudes, respectively, and ZP are the photometric zero-points for each band. K_{MK} is the corresponding mean atmospheric extinction at Mauna Kea, obtained from the Gemini Observatory Web Page¹ and X is the airmass. For the g' filter, part of the programme was scheduled in February, while the rest of the observations were obtained a month later, together with a photometric standards field. The zero-points for February and March observations were $ZP^{g'} = 28.29 \pm 0.03$ and $ZP^{g'} = 28.30 \pm 0.03$, respectively. The final assumed zero-points for the g' , r' and i' filters were $ZP^{g'} = 28.30 \pm 0.03$, $ZP^{r'} = 28.38 \pm 0.02$ and $ZP^{i'} = 28.49 \pm 0.03$, respectively. In the next step, we applied the Galactic extinction corrections obtained from Schlafly & Finkbeiner (2011) to the calibrated magnitudes. Finally, considering the point-sources common in both fields N3610F and WestF, we calculated the following zero-point differences, $\Delta_{g'} = -0.06$, $\Delta_{r'} = 0.10$ and $\Delta_{i'} = 0.13$. We applied these offsets to the WestF catalogue and referred the photometry to the field N3610F.

In the case of ACS data, the calibrated magnitudes were obtained using the relation:

$$m_{\text{std}} = m_{\text{inst}} + ZP$$

for each filter, with zero-points $ZP_{F555} = 25.724$ and $ZP_{F814} = 25.501$, taken from Sirianni et al. (2005), so that the

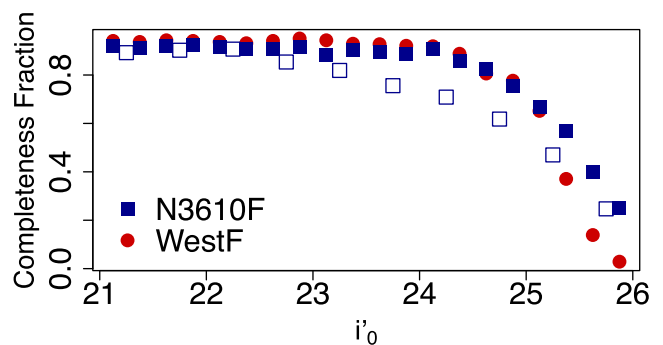


Figure 2. Completeness curves for the two GMOS fields, as function of i'_0 magnitude. The bin width is 0.25 mag. For the field N3610F, we distinguished between artificial stars at less than 1 arcmin from NGC 3610 centre (open squares), and further than this limit (filled squares).

resulting calibrated magnitudes correspond to V and I filters, respectively.

The ACS data have already been used to study the properties of the GC candidates by Goudfrooij et al. (2007), who applied along their work corrections for contamination by background objects. Such contamination was calculated as the compact objects detected beyond a galactocentric radius (hereafter designated with ' R_g ') $R_g = 100$ arcsec (i.e. 1.67 arcmin), which they considered might be slightly overestimated. In fact, thanks to the larger area covered by our GMOS data, we will show in the following that GCs are present up to $R_g = 4$ arcmin. Thus, it is worth doing a new analysis of the ACS data, together with the new ones from GMOS, but taking into account a more precise estimation of the correction for background contamination.

In order to estimate the background contamination for the GMOS data, we considered the point-sources within an area of 16.5 arcmin^2 at the western side of field WestF, located at ~ 5 arcmin from the centre of NGC 3610. It will be identified in the following as the 'comparison region'. As we lack an appropriate comparison field for the ACS data, we will use the corrections obtained from the comparison region of the GMOS data, taking into account the different depths and completeness corrections of both photometries.

2.4 Completeness analysis

In order to estimate the photometric completeness for our GMOS fields, we added 250 artificial stars to the images of the three filters, distributed over the entire fields in an homogeneous way. Their colours span the expected ranges for GCs and magnitudes equally generated for $21 < i'_0 < 26$. As this process was repeated 40 times, we achieved a whole sample of 10 000 artificial stars. Their photometry was performed following exactly the same steps as for the science images. After selecting the definite point-sources, we obtained the completeness curves shown in Fig. 2. For the field N3610F, we discriminated between artificial stars located at less than 1 arcmin from the NGC 3610 centre (open squares), and further than this limit (filled squares). The completeness functions for the outer region of N3610F and the field WestF are very similar, achieving the 70 per cent at $i'_0 \sim 25$. This value has been considered as the faint magnitude limit in the following analysis.

In the case of the ACSF field, we added 50 artificial stars per image, spanning the colour range of GCs and $21.5 < I_0 < 27$. We repeated the process to achieve a final sample of 50 000 artificial stars, which allowed us to calculate the completeness curves for

¹ <http://www.gemini.edu/sciops/instruments/gmos/calibration>

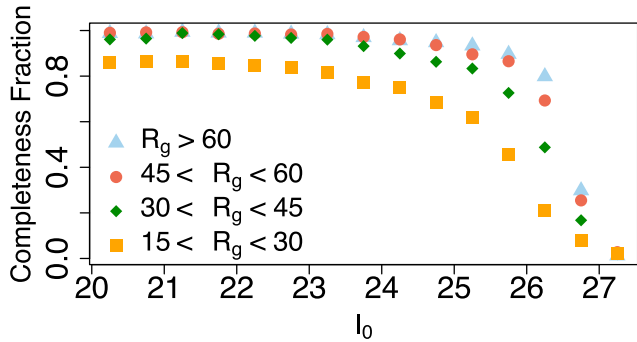


Figure 3. Completeness curves for the ACSF, as a function of I_0' magnitude, for different galactocentric ranges (R_g in arcsec). The bin width is 0.25 mag.

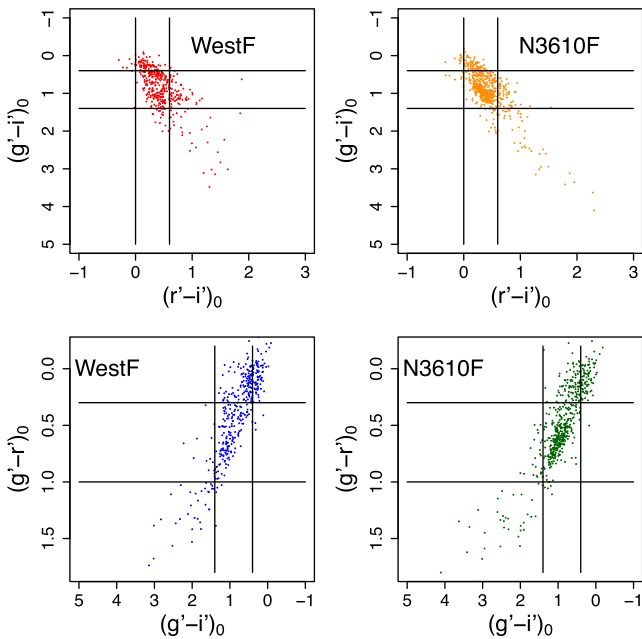


Figure 4. Colour–colour diagrams for both GMOS science fields. Solid lines indicate the colour ranges of selected GC candidates (see Section 3.1).

different galactocentric ranges (Fig. 3). As well as for the GMOS fields, the photometry was developed in the same manner as for the science field. We selected as magnitude limit $I_0 \sim 25.5$, which might represent a conservative selection for the outer galactocentric ranges, but corresponds to ~ 60 per cent in the range $15 \text{ arcsec} < R_g < 30 \text{ arcsec}$. For the GMOS and ACS fields, it is clear the decrease of the completeness as we approach the galaxy centre.

3 GLOBULAR CLUSTER SYSTEM OF NGC 3610

3.1 Selection of GC candidates

The colour–colour diagrams $(g' - i')_0$ versus $(r' - i')_0$ and $(g' - r')_0$ versus $(g' - i')_0$ for all the point-sources in both GMOS fields are presented in Fig. 4. As the colours of bona fide GCs fall within narrow ranges, we can use these diagrams to distinguish them from the contamination (e.g. Caso et al. 2015, and references therein). We selected as GC candidates the point-sources in the following ranges: $0.4 < (g' - i')_0 < 1.4$, $0.3 < (g' - r')_0 < 1$ and $0 < (r' - i')_0 < 0.5$.

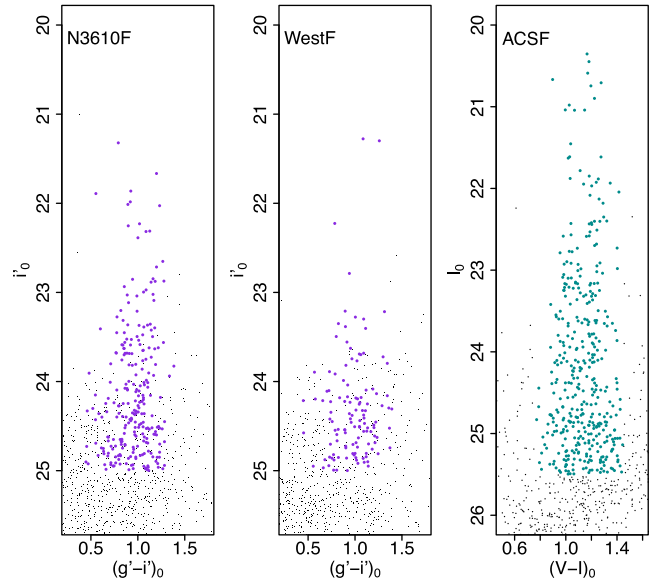


Figure 5. CMDs for the two GMOS fields and the ACS field. Filled circles highlight those objects that fulfil the colours and magnitude criteria applied to select GC candidates.

These adopted limiting colours are similar to those chosen by Caso et al. (2015) and Escudero et al. (2015).

Strader et al. (2003, 2004) inferred ages and metallicities for a sample of 13 GC candidates in NGC 3610, by means of Lick/IDS indices, resulting in a majority of old GCs. However, two GC candidates in their sample turned out to be young and very metal rich ($\sim 2 \text{ Gyr}$ and $[Z/H] \sim 0.5$). In order to confirm that even these GCs would be identified with the present selection criteria, we obtained the expected colours in our bandpasses from the theoretical models of single stellar populations (SSP) by Bressan et al. (2012), using their web-based tool.² If we consider a Chabrier (2001) lognormal initial mass function (IMF) and the reddening corrections applied to our point-sources catalogue, an SSP with these ages and metallicities would have $(g' - i')_0 \sim 1$, $(g' - r')_0 \sim 0.7$ and $(r' - i')_0 \sim 0.3$, which fulfil our colour criteria.

In the ACS photometry, we selected as GC candidates the point-sources or marginally resolved sources with colours ranging $0.75 < (V - I)_0 < 1.4$ (Bassino, Richtler & Dirsch 2008). In Fig. 5, the left-hand side and middle panels show the i'_0 versus $(g' - i')_0$ colour–magnitude diagrams (CMD) for the two GMOS fields. The black dots represent the objects that fulfil the point-source criteria, after the χ and sharp selection. The filled circles identify those that fulfil the GC candidates’ colours and magnitude criteria indicated before. The right-hand side panel shows the I_0 versus $(V - I)_0$ CMD for the ACS field, with GC candidates highlighted with filled circles.

In order to calculate the (V, I) to (g', i') transformation, we selected the 62 GC candidates with available colours in both photometric systems, with $i'_0 < 24 \text{ mag}$. Fig. 6 shows $(g' - i')_0$ versus $(V - I)_0$ colours for these objects. The solid line represents the transformation obtained with a linear least-squares fit,

$$(g' - i')_0 = 1.26 \pm 0.06 \times (V - I)_0 - 0.43 \pm 0.07. \quad (1)$$

As a comparison, from an equivalent transformation presented by Faifer et al. (2011), their equation (3), we can derive the coefficients

² <http://stev.oapd.inaf.it/cgi-bin/cmd>

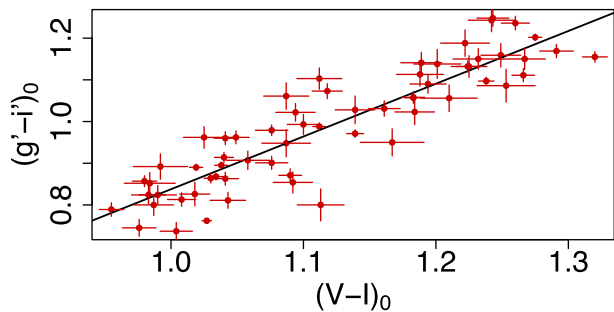


Figure 6. $(g' - i')_0$ versus $(V - I)_0$ colours for a sample of bright GC candidates with available magnitudes in both photometric systems.

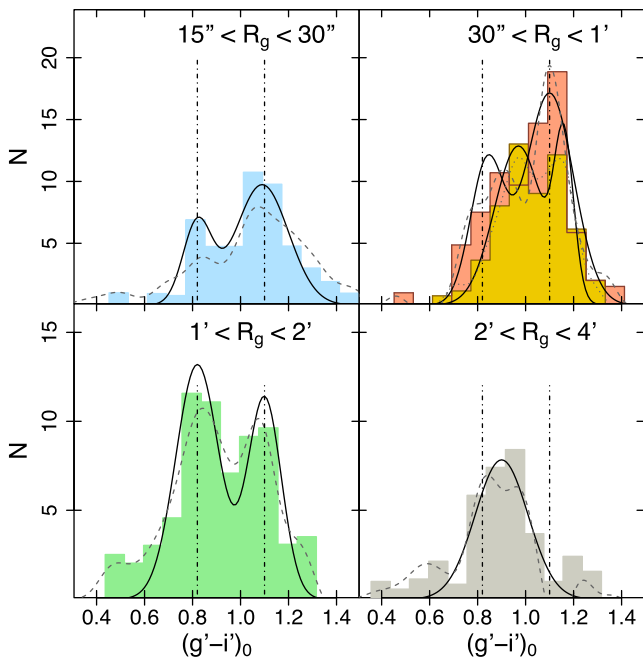


Figure 7. Background-corrected colour distribution (dashed lines) for the GC candidates from ACS photometry (upper left panel), overlapping ACS and GMOS data (upper right panel, GMOS sample is the smaller one), and GMOS photometry (lower panels), for four radial intervals as indicated in the respective panels. Solid lines show the results from GMM fitting and vertical dot-dashed lines indicate the typical colours of blue and red peaks [$(g' - i')_0 = 0.82$ and 1.10 , respectively]. Please, note the different scales in upper and lower panels.

1.25 and 0.4, respectively. According to this transformation, we improve our GC colour limits as $0.66 < (V - I)_0 < 1.45$ so that they agree with the ones adopted for $(g' - i')_0$. Between I_0 and i'_0 there is only a zero-point difference,

$$i'_0 = I_0 + 0.43 \pm 0.01. \quad (2)$$

3.2 Colour distribution

In order to analyse the GC colour distribution, we separated the sample in four radial regimes, corresponding to $15 < R_g < 30$ arcsec, $30 \text{ arcsec} < R_g < 1$ arcmin, $1 < R_g < 2$ arcmin and $2 < R_g < 4$ arcmin. To this aim, we combined GMOS and ACS data, transforming ACS photometry into $(g' - i')_0$ colour and i'_0 magnitude by means of equations (1) and (2). Both data sets will overlap in only one radial range ($30 \text{ arcsec} < R_g < 1$ arcmin). Fig. 7 shows the background-corrected

$(g' - i')_0$ colour distribution (dashed lines) for GC candidates in these four different radial ranges, with $i'_0 < 25$ and applying a bin width of 0.08 mag.

The same procedure was applied in the four radial ranges. First, we obtained a clean sample of GC candidates, randomly selecting sources from the comparison region and deleting GC candidates with similar $(g' - i')_0$ colours, until we reached the expected number of objects due to contamination. Then, we applied to each sample the Gaussian Mixture Modelling (GMM) test (Muratov & Gnedin 2010) to determine whether their respective colour distributions are likely to be represented by the sum of two Gaussians. For each case, this procedure was repeated 25 times, and the mean results are listed in Table 1, including the mean colours, dispersions, and the fractions (f) for each subpopulation. The two last columns correspond to the DD parameter, which is related to the separation of the mean values and indicates whether a specific bimodal distribution provides a realistic fit (a meaningful bimodal case is accepted for $DD > 2$), and the kurtosis (κ), which is expected to be negative for bimodal distributions. For the sake of comparison, we have included in Table 1 the results of the unimodal fits even in the cases where DD and κ pointed to a bimodal fit. According to the calculated DD and κ parameters, the three inner subsamples seem to be better described by bimodal distributions, but just a single Gaussian should be fitted to the outermost one. Moreover, it is also noticeable from Fig. 7 how different the GC colour distributions are when we discriminate them according to R_g .

For the inner radial subsample, $15 < R_g < 30$ arcsec, the colour distribution is better fitted by two Gaussians, with expected values for the blue and red peaks (mean colours), i.e. $(g' - i')_0 \sim 0.8$ and 1.1 (e.g. Escudero et al. 2015). This distribution is dominated by the red GC subpopulation that represents more than 70 per cent of the subsample. The GC distribution for $30 \text{ arcsec} < R_g < 1$ arcmin is also better fitted by two Gaussians, as indicated by the DD and κ parameters for both ACS and GMOS data. Both distributions are shown in Fig. 7 (upper right panel) and the histograms look similar, with a dominant red subpopulation and a few more GCs in the ACS sample. However, the fits are not so similar, as only the ACS data have blue and red peaks in agreement with the ones estimated for the previous (innermost) radial range. The colour of the bluer peak estimated for the GMOS subsample is in the middle between the usual blue and red peaks, though it must be taken into account that the differences may be due to few GCs. Anyway, the colour distribution for both subsamples of ACS data agrees with that for the inner subsample of GMOS data, in the sense that they are all dominated by red GCs. This is also evident from the radial projected distribution depicted in Fig. 9 (middle panel), where there is a clear deficiency of blue GCs in the inner region as compared to the profile for larger R_g .

The intermediate radial GMOS subsample (lower left panel) shows the more clear bimodal distribution, with blue and red peaks in the expected colours (indicated in all panels with dot-dashed vertical lines to facilitate comparison). The fractions of blue and red clusters are 60 and 40 per cent, respectively, with the blue subpopulation presenting an extension towards very blue colours. Finally, the outermost GMOS subsample (lower right panel) is quite anomalous as a unimodal distribution is present, with a mean $(g' - i')_0 = 0.87$. We are aware that this is a small subsample, where a bunch of blue clusters also seems to be present, but the group is dominated by GCs of ‘intermediate’ colours. Their mean colour agrees with the bluer peak obtained for the inner GMOS subsample ($30 \text{ arcsec} < R_g < 1$ arcmin), so they may be probable present at smaller radii too. We have already detected GCs of ‘intermediate’ colours

Table 1. Parameters of the gMM fitting to the colour distribution, considering different radial ranges. μ_j , σ_j and f_j correspond to the mean, dispersion and fraction for each Gaussian component ($j = 1$: blue GCs and $j = 2$: red GCs). We refer to the text for the meanings of DD and κ .

	μ_1	σ_1	f_1	μ_2	σ_2	f_2	DD	κ
ACS data								
15 arcsec $< R_g < 30$ arcsec							3.19 ± 0.46	-0.67
Unimodal	1.03 ± 0.02	0.15 ± 0.01	–	–	–	–		
Bimodal	0.82 ± 0.03	0.06 ± 0.02	0.27 ± 0.09	1.09 ± 0.03	0.11 ± 0.02	0.73 ± 0.09		
30 arcsec $< R_g < 1$ arcmin							2.89 ± 0.45	-0.81
Unimodal	1.02 ± 0.02	0.15 ± 0.01	–	–	–	–		
Bimodal	0.84 ± 0.03	0.07 ± 0.02	0.32 ± 0.11	1.10 ± 0.02	0.10 ± 0.02	0.68 ± 0.11		
GMOS data								
30 arcsec $< R_g < 1$ arcmin							2.15 ± 0.17	-0.55
Unimodal	1.03 ± 0.01	0.13 ± 0.01	–	–	–	–		
Bimodal	0.97 ± 0.03	0.10 ± 0.01	0.72 ± 0.05	1.16 ± 0.02	0.04 ± 0.01	0.28 ± 0.05		
1 arcmin $< R_g < 2$ arcmin							3.15 ± 0.13	-0.97
Unimodal	0.93 ± 0.01	0.16 ± 0.01	–	–	–	–		
Bimodal	0.82 ± 0.02	0.09 ± 0.01	0.60 ± 0.03	1.10 ± 0.01	0.07 ± 0.01	0.40 ± 0.03		
2 arcmin $< R_g < 4$ arcmin							1.82 ± 0.20	
Unimodal	0.87 ± 0.02	0.11 ± 0.01	–	–	–	–		

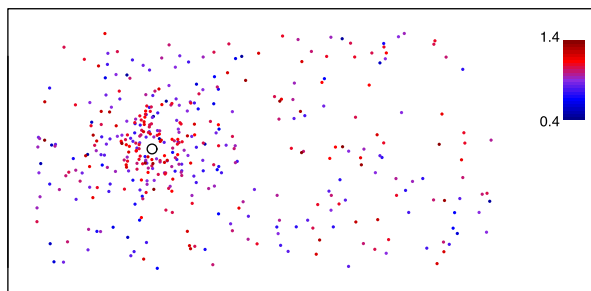


Figure 8. Projected spatial distribution for GC candidates from ACS and GMOS data. The centre of the galaxy is highlighted with an open circle. North is up, east to the left. The field of view is 10.2×5.5 arcmin². The colour bar depicted on the top right-hand side corresponds to $(g' - i')$.

in other galaxies that experienced recent mergers, and will come back to this in the Discussion.

Summarizing, thanks to the larger FOV of GMOS, we have been able to study the GC colour distribution over the whole radial extent, reaching the outer subpopulations never analysed before. We recovered the dominant inner red GC subpopulation in agreement with the results from the ACS data, and found a bimodal GC distribution at intermediate radii as well as a small number of clusters with ‘intermediate’ colours in the outskirts, though they may be present at inner regions too.

3.3 Projected spatial and radial distributions

The projected spatial distribution for GC candidates in both GMOS fields, combined with those selected from the ACS data in the inner region, is shown in Fig. 8. The colour range, as depicted in the figure, spans $0.4 < (g' - i')_0 < 1.4$ and the centre of NGC 3610 is indicated with an open circle. It can be seen that red GCs are more concentrated towards the galaxy, while clusters of bluer colours appear to dominate at larger radii.

Fig. 9 presents the raw and background-corrected radial distributions for the GC candidates from GMOS data (open and filled circles, respectively), and corrected by completeness. The open and filled triangles represent the analogous distributions, but from ACS data. Upper panel corresponds to the whole GC sample, while middle and lower panels present similar plots but for blue and red

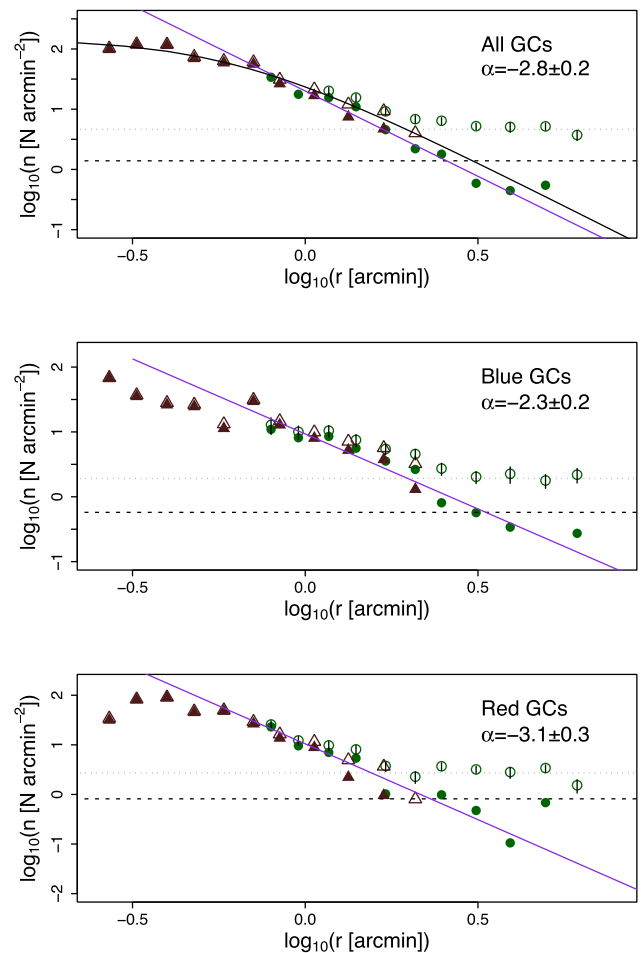


Figure 9. Raw and background-corrected radial distributions for GC candidates (open and filled circles, respectively). Triangles and circles identify the combined data, from ACS and GMOS, respectively. The solid straight lines represent the respective power laws, fitted by least-squares, and the respective slopes α are depicted in each panel. The dashed lines correspond to the respective background levels, while the dotted ones indicate 30 per cent of the background level, used to define the GCS extension. The solid curved line in the upper panel shows the fit of a Hubble profile (see text for the results). Please, note the different scale in the lower panel.

GCs, respectively. It can be seen that results from GMOS and ACS data are in good agreement within the range of overlapping R_g . Here, we do not consider separately the intermediate colour clusters (located in the outer region) as they are too few to derive a radial profile. The adopted colour limit between both GC subpopulations is $(g' - i')_0 = 0.95$ (Faifer et al. 2011), which corresponds to $(V - I)_0 = 1.1$. The respective background levels are indicated with dashed lines, and were determined from the comparison region described in Section 2.3.

The background-corrected radial profiles were fitted by power laws with slopes -2.8 ± 0.2 , -2.3 ± 0.2 and -3.1 ± 0.3 for the entire sample, blue and red GCs, respectively (indicated with the solid lines). Due to incompleteness in the central region, the fits were performed for radii $0.5 < r < 4$ arcmin. These results clearly confirm that the red subpopulation is more concentrated towards the galaxy while the bluer clusters one extends further away.

We established the GCS extent as the galactocentric distance at which the background-corrected surface density is equal to the 30 per cent of the background level (dotted lines). This criterion has been previously used in similar studies (e.g. Bassino et al. 2006), and implies a new determination of the GCS extent of ~ 4 arcmin, i.e. ~ 40 kpc at the adopted distance for NGC 3610.

For both GC subpopulations, the radial density profiles flatten towards the galaxy centre. As the completeness analysis was performed for different galactocentric radii, in order to take into account the effect of the galaxy surface-brightness profile, the flattened radial profiles might imply a real paucity of GCs in the inner regions of the galaxy. In order to consider the slope change, we fitted to the radial profile of the entire sample ($r < 4$ arcmin) a Hubble profile (Binney & Tremaine 1987; Dirsch et al. 2003) of the form:

$$n(r) = a \left(1 + \left(\frac{r}{r_0} \right)^2 \right)^b, \quad (3)$$

where $a = 152 \pm 13$, $r_0 = 0.62 \pm 0.05$ and $b = -1.42 \pm 0.08$ (solid curved line in Fig. 9, upper panel). This profile provides a much better fit to the inner radial distribution. As well as GCs formation requires specific environmental conditions and merger remnants are the places where young massive clusters (YMCs) are found (e.g. Kruijssen 2014), these conditions also favour their tidal disruption (Kruijssen et al. 2012; Kruijssen 2015). Brockamp et al. (2014) also points to the relevance of the erosion of GCs in the present-day characteristics of its GCS. The erosion might be responsible for the evolution of GCs mass function from the initial power law to a bell-shaped distribution. The GCs destruction mainly occurs up to the galaxy half-light radius, with smaller upper limit radius and efficiency when we move towards more massive and extended elliptical galaxies. The degree of the initial radial anisotropy in the velocity distribution of the GCS also play a main role in the fraction of eroded GCs and the radius at which it is efficient (Brockamp et al. 2014).

3.4 Luminosity function and GC population

Fig. 10 shows the background and completeness corrected GCLF for the GC candidates selected from the GMOS data. The errorbars assume Poisson uncertainties for science and background measurements, and the bin width is 0.25 mag. The bins filled with vertical grey lines have not been considered in the GCLF fitting, due to the declining completeness (i.e. according to the limit $i'_0 = 25$ adopted in Section 2.4). The turnover magnitude (TOM) and

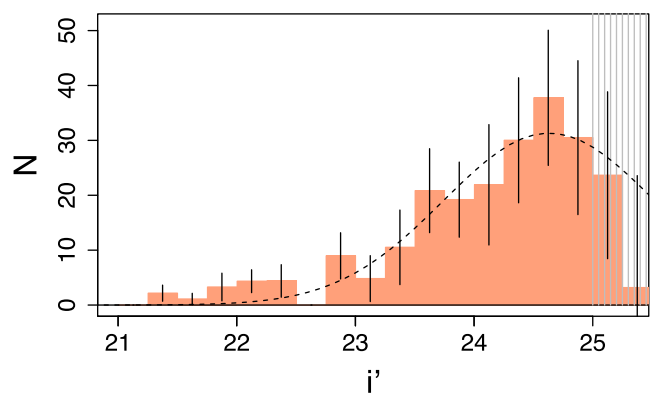


Figure 10. Background- and completeness-corrected luminosity function (GCLF) for GCs based on the GMOS data. The errorbars assume Poisson uncertainties for science and background measurements, and the bin width is 0.25. The vertical lines indicate the luminosity range fainter than $i'_0 = 25$, that has not been included in the GCLF fitting.

dispersion obtained from the least-squares fit of a Gaussian model are $i'_{0,\text{TOM}} = 24.6 \pm 0.25$ and $\sigma = 0.9 \pm 0.24$.

Old GC populations in early-type galaxies usually present a Gaussian GCLF, with a TOM in the V band of $M_{V_{\text{TOM}}} \sim -7.4$ (e.g. Richtler 2003; Jordán et al. 2007), denoting the universality of the GCLF that is a reliable distance indicator. On the basis of ACS data, Goudfrooij et al. (2007) found that the GCLF for red GCs in NGC 3610 deviates from the usual Gaussian distribution and can be fitted by a power law. It has been clearly shown that power-law luminosity functions correspond to young stellar clusters, not bona fide old GCs (e.g. Whitmore et al. 2014). Our GMOS photometry is not as deep as the ACS one, so we cannot compare directly the behaviour of both GCLFs. In addition, if we want to use the ACS photometry that we have re-done, the background correction to be applied to these data was obtained from the GMOS images, so the same limiting magnitude is valid.

We have adopted for NGC 3610 the SBF distance modulus ($m - M \sim 32.7$), which implies a ‘standard’ $V_{\text{TOM}} \sim 25.3$ according to the $M_{V_{\text{TOM}}}$ quoted above. If we use the colour and magnitude transformations derived in Section 3.1 and consider for the GC candidates a mean colour $(g' - i') \sim 0.96$ (estimated from a clean sample), the resulting TOM is $i'_0 \sim 24.6$, in agreement with the value obtained directly from the data. As we are analysing the global GCLF, and not those of blue and red GCs separately, the TOM from the fitted Gaussian agrees with what would be a ‘standard’ TOM, according to the SBF distance. We understand this result as just a consequence that we are considering the whole GC sample, which is dominated by truly ‘old’ GCs, and we are not able to study separately the LF of the intermediate-age GC subpopulation.

In order to estimate the total GC population, with the advantage of having a large FOV with the GMOS data, we first consider the number of GCs obtained from the integration of the Hubble radial profile. Then, we apply a correction to take into account that we are covering a fraction of the fiducial Gaussian adopted as GCLF, up to our magnitude limit $i'_0 \sim 25$. With this procedure, the estimated ‘old’ GC population of NGC 3610 results 500 ± 110 members.

Assuming the total V_0 magnitude of NGC 3610, obtained from NED, as $V_{\text{tot}_0} = 10.7 \pm 0.13$, and the distance modulus $m - M = 32.7 \pm 0.1$, the absolute V magnitude of the galaxy is $M_V = -22.0 \pm 0.16$. Then, the specific frequency, i.e. the number of GCs per unit galaxy luminosity (Harris & van den Bergh 1981), for the old GC population results $S_N = 0.8 \pm 0.4$. It is approximately in

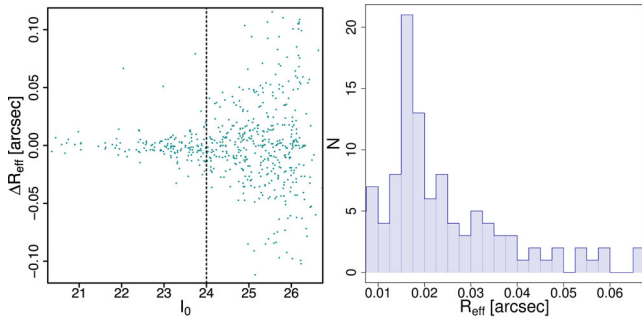


Figure 11. Left: difference between R_{eff} measured in V and I filters for GC candidates from ACS data, in arcsec. The vertical dashed line represents the magnitude limit up to which R_{eff} is reliable. Right: R_{eff} distribution for GC candidates brighter than $I_0 = 24$.

agreement, within the errors, with the specific frequencies obtained by Whitmore et al. (1997, $S_N = 0.6 \pm 0.14$) and Goudfrooij et al. (2007, $S_N = 1.4 \pm 0.6$). Such values correspond to the lower limit of the range of S_N obtained for elliptical galaxies of similar luminosity (Harris et al. 2013). In fact, the most frequent galaxy type with $S_N < 1$, in the brightness range corresponding to massive galaxies ($M_V < -20$), are not ellipticals but spirals (Harris et al. (2013), their fig. 10).

3.5 Effective radii of globular clusters

The size of GCs, measured as their effective (R_{eff}) or half-light radius, is one of the parameters that characterize these stellar systems and helps our understanding of their formation and evolution (e.g. Puzia et al. 2014, and references therein). As a consequence of the outstanding resolution of the ACS data, it is possible to compute R_{eff} of GCs up to few parsecs, at similar distances than NGC 3610 (e.g. Caso et al. 2013a, 2014). For this purpose, we used the software ISHAPE (Larsen 1999), designed to calculate structural parameters for marginally resolved objects by fitting their surface-brightness profiles with analytical models, convolved with a PSF. As mentioned in Section 2.2, for each filter we derived the PSF from observations of 47 Tuc outskirts, with images obtained during the same month as those of NGC 3610. We selected a King30-profile, i.e. a King profile with concentration parameter $c = 30$, being c the ratio of tidal over core radius (King 1962, 1966). We did not consider any possible eccentricity, but large values are not expected for GCs nor for UCDs (e.g. Harris 2009; Chiboucas et al. 2011). The left-hand panel of Fig. 11 shows the difference between the R_{eff} measured in V and I for the GC candidates as a function of I_0 , which presents an even distribution around zero. The mean R_{eff} between those obtained in both filters will be adopted as the final values. Larsen (1999) indicated that structural parameters calculated by ISHAPE are reliable when the object R_{eff} is at least one-tenth of the PSF, for $S/N \sim 50$ or higher. This latter condition is fulfilled in both filters for GCs brighter than $I_0 = 24$, indicated with a vertical dashed line in the figure. In both filters, the derived PSF had FWHM ~ 0.08 arcsec, which implies for the King30-profile $R_{\text{eff}} \sim 0.12$ arcsec. Hence, reliable R_{eff} measurements were obtained for GCs brighter than $I_0 = 24$ and with $R_{\text{eff}} > 0.01$ arcsec. This agrees with the results, as small differences in the R_{eff} calculated with both filters were obtained for GCs brighter than the quoted magnitude limit.

The right-hand panel of Fig. 11 shows the R_{eff} distribution for GC candidates brighter than $I_0 = 24$. The bin width is 0.0025 arcsec. The

distribution maximum is about 0.015–0.0175 arcsec (~ 0.35 pixels), which corresponds to 2.5–3 pc at the distance of NGC 3610, i.e. similar to the mean R_{eff} obtained with ACS data for GCs in nearer early-type galaxies, like the ones in Virgo and Fornax clusters (e.g. Jordán et al. 2005; Masters et al. 2010).

In order to explore relations between size, colour and luminosity of GCs, the left-hand panel of Fig. 12 shows R_{eff} versus M_V for the 13 clusters in NGC 3610 spectroscopically confirmed by Strader et al. (2003, 2004, highlighted with open circles), together with GCs/UCDs from Virgo (Brodie et al. 2011), Fornax (Mieske et al. 2004), Antlia (Caso et al. 2013a, 2014), Hydra (Misgeld et al. 2011) and Coma (Chiboucas et al. 2011). The colour bar represents $(V - I)_0$ colours. For Virgo objects, the colour was obtained from $g'i'$ -band photometry applying the transformations derived in this paper. As expected, there seems to be no correlation between mean size and luminosity for the M_V range of typical GCs (e.g. Puzia et al. 2014), excluding the so-called extended clusters (EC). The ECs have similar brightness than GCs but present larger sizes, i.e. $R_{\text{eff}} > 10$ pc (Brüns & Kroupa 2012; Forbes et al. 2013, and references therein). For brighter objects, in the UCD's domain, the size globally increases with luminosity (Brüns & Kroupa 2012; Norris et al. 2014).

Among the NGC 3610 confirmed clusters (Strader et al. 2004), and according to the $(V - I)$ colour limits adopted in this paper, two clusters are blue, eight clusters are red and three have intermediate colours. Table 2 gives their magnitudes and colours from the $g'i'$ -band photometry calculated in this paper, as well as their estimated effective radii and corresponding errors. All of them have radii in the range of typical GCs with the exception of a single object, spectroscopically confirmed and identified as W30 (Strader et al. 2003), that is marginally larger ($R_{\text{eff}} = 11.55$ pc) and might be classified as EC. The two young and metal-rich clusters are in the reddest subsample, with sizes $R_{\text{eff}} = 3.22$ and 7.36 pc for W6 and W11, respectively.

The right-hand panel of Fig. 12 presents an analogue plot but for NGC 3610 GC candidates, including the 13 spectroscopically confirmed clusters (identified with open circles). Several EC candidates are also present, within the luminosity range typical of GCs. As quoted above, the cluster named W30 is included among them. This EC has intermediate colours and, according to the Lick/IDS analysis performed by Strader et al. (2004), it has a typical GC-like age. There is a small group of both confirmed objects and candidates on the bright side, close to $M_V \sim -11$, which are in the brightness limit between massive GCs and UCDs. The young metal-rich clusters W6 and W11 are located in the same place as this group and, comparing with the analogous plot presented by Norris et al. (2014) in their fig. 11, they may fall on an extension of the sequence of YMCs towards fainter and smaller clusters. As part of this group, there are three GC-like objects with available R_{eff} measurements and whose positions match with X-ray point-sources from Liu (2011, identified with open triangles). Out of these latter objects, one is the spectroscopically confirmed GC identified as W9 by Strader et al. (2003). From the Lick/IDS indices, these authors showed that W9 is old and red (metal-rich), with metallicity $[\text{Fe}/\text{H}] = -1.2 \pm 0.2$. The two remaining GC candidates lack spectroscopic confirmation, but their photometric ages and metallicities were derived by Georgiev et al. (2012). They correspond to young objects: G8, ~ 2 Gyr and $[Z/H] \sim -0.2$, and G14, ~ 5 Gyr and $[Z/H] \sim -0.4$.

Thus, most of the GC candidates brighter than $I_0 = 24$ have sizes in the expected range for GCSs of nearby early-type galaxies, but we also detected a group of ECs. Among the 13 spectroscopically confirmed GCs, only one seems to be an EC and the rest have normal

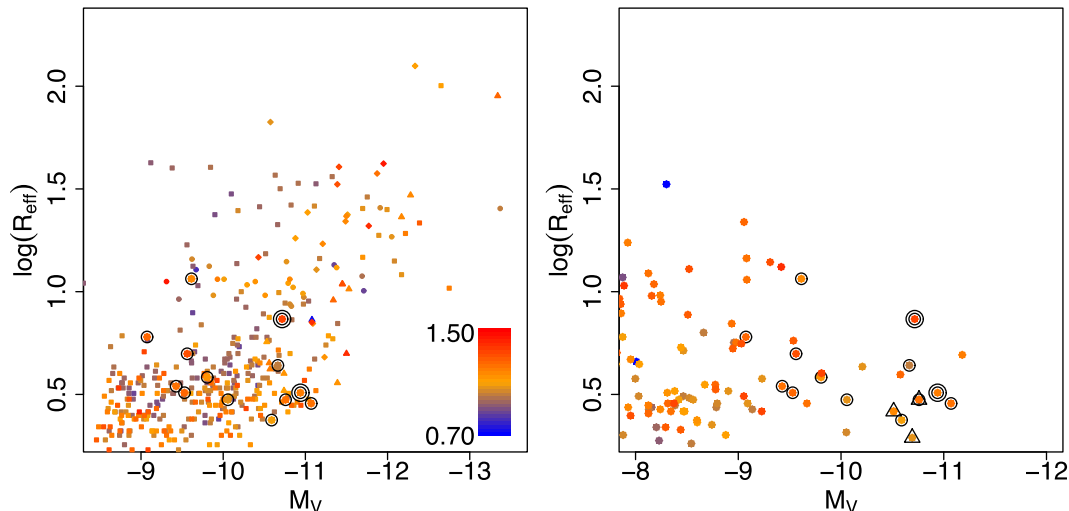


Figure 12. Left: R_{eff} (pc) versus M_V for NGC 3610 spectroscopically confirmed GCs (Strader et al. 2003, 2004, highlighted with open circles), together with GCs/UCDs from Virgo (Brodie et al. 2011), Fornax (Mieske, Hilker & Infante 2004), Antlia (Caso et al. 2013a, 2014), Hydra (Misgeld et al. 2011) and Coma (Chiboucas et al. 2011). The two clusters identified with double circles correspond to W6 and W11, the young and metal-rich ones from the Strader sample. Right: similar plot for NGC 3610 GC candidates, including the same spectroscopically confirmed GCs (open circles), and three GC-like objects with available R_{eff} measurements (triangles), whose positions match with X-ray point-sources (Liu 2011). The colour bar represents the $(V - I_0)$ colours of GCs and UCDs in both panels.

Table 2. Magnitudes, colours (from GMOS data), and effective radii for the spectroscopically confirmed clusters (Strader et al. 2004). Identifications (ID) are taken from Strader et al. (2003, 2004).

ID	i'_0 (mag)	$(g' - i'_0)$ (mag)	R_{eff} (pc)
W3	20.84 ± 0.01	1.07 ± 0.01	2.86 ± 0.77
W6	21.01 ± 0.01	1.06 ± 0.01	3.22 ± 0.09
W9	21.09 ± 0.02	0.98 ± 0.02	2.97 ± 0.09
W10	21.39 ± 0.01	0.92 ± 0.02	4.38 ± 0.17
W11	21.24 ± 0.01	1.20 ± 0.01	7.36 ± 0.26
W12	21.48 ± 0.01	0.94 ± 0.01	2.37 ± 0.26
W22	22.01 ± 0.01	0.89 ± 0.02	2.98 ± 0.26
W28	22.23 ± 0.01	1.02 ± 0.02	3.83 ± 0.09
W30	22.39 ± 0.01	1.00 ± 0.02	11.55 ± 0.34
W31	22.44 ± 0.01	1.15 ± 0.02	4.98 ± 0.68
W32	22.43 ± 0.01	1.14 ± 0.02	3.22 ± 0.26
W33	22.60 ± 0.01	0.97 ± 0.02	3.47 ± 0.60
W40	22.84 ± 0.01	1.16 ± 0.02	6.02 ± 0.60

GC sizes. In particular, one of the two young and metal-rich ones (W11, $R_{\text{eff}} = 7.36$ pc) is marginally larger than the mean.

4 SURFACE PHOTOMETRY OF NGC 3610

Fig. 13 shows the surface-brightness profile of NGC 3610 (surface brightness versus equivalent radius, being $r_{\text{eq}} = \sqrt{ab} = a\sqrt{1 - \epsilon}$, where a is the isophote semimajor axis and ϵ its ellipticity) in the g' filter, obtained with the IRAF task ELLIPSE. The galaxy profile has been fitted with two Sérsic models (Sérsic 1968) expressed in surface-brightness units (mag arcsec^{-2})

$$\mu(r) = \mu_0 + 1.0857 \left(\frac{r_{\text{eq}}}{r_0} \right)^{1/n}, \quad (4)$$

where μ_0 is the central surface brightness, r_0 is a scale parameter and n is the Sérsic shape index (i.e. $n = 1$ corresponds to an exponential profile and $n = 4$ to a de Vaucouleurs profile). The re-

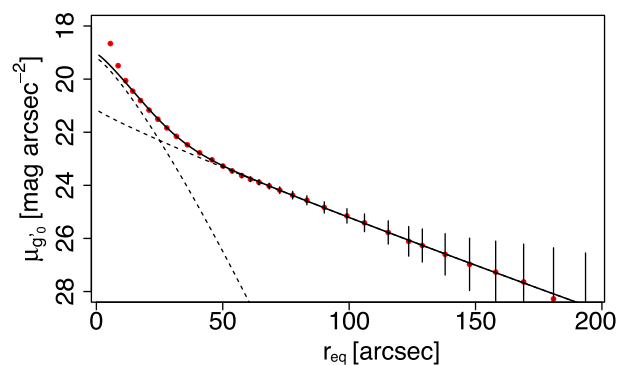


Figure 13. Surface-brightness profile of the NGC 3610, g' band. The dashed lines represent two Sérsic models fitted to the galaxy profile, while the solid line indicates the sum of them.

Table 3. Parameters of the two Sérsic models fitted to the galaxy profile in the g' filter. Both r_0 and r_{eff} are expressed in arcsec.

Component	μ_0	r_0	n	r_{eff}
Inner	19.2 ± 0.2	10.6 ± 1.3	0.8 ± 0.08	13.6
Outer	21.1 ± 0.2	23.2 ± 2.8	1.1 ± 0.05	47.3

sulting parameters for the inner and outer components are listed in Table 3, where we have also included the respective effective radii, according to the relation

$$r_{\text{eff}} = b_n^n r_0, \quad (5)$$

where b_n is a function of the n index, that may be estimated with the expression given by Ciotti (1991).

If we compare our two-component fit with the photometric analysis performed by Whitmore et al. (1997, 2002), we are not able to detect their small twisted ‘inner disc’ within 3 arcsec (Whitmore et al. 2002). We just attempt to fit the inner part excluding the very central 20 arcsec, where the profile gets steeper, as we are mostly interested in the large-scale brightness distribution.

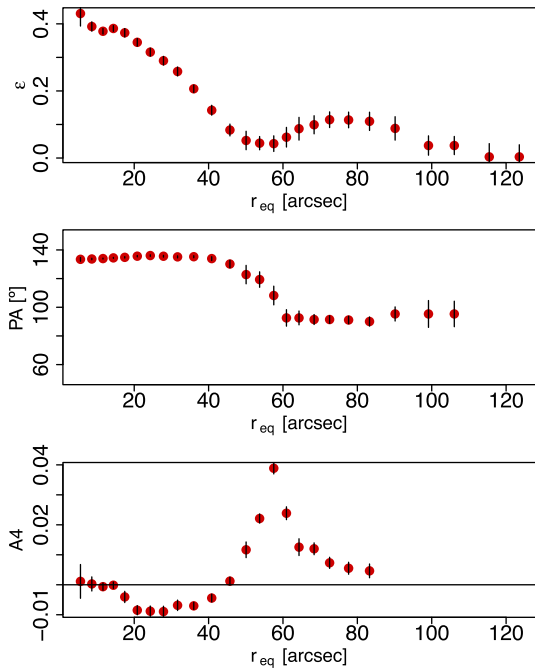


Figure 14. Ellipticity ϵ , position angle PA and A4 Fourier coefficient of the elliptical isophotes versus equivalent radius r_{eq} .

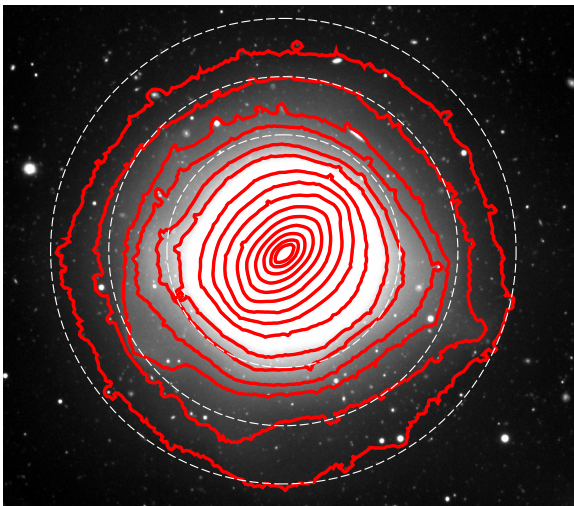


Figure 15. GMOS image of NGC 3610 (N3610F) in the g' band with light contours overplotted in red (solid lines). Three concentric circles (dashed lines) are shown at 60, 90 and 120 arcsec from the galaxy centre, in order to facilitate the comparison with other figures and the text.

Fig. 14 shows the parameters obtained with ELLIPSE that characterize the fitted elliptical isophotes: ellipticity ϵ , position angle PA (measured positive from N to E), and the A4 Fourier coefficient that is related to diskiness ($A4 > 0$ discy isophotes, $A4 < 0$ boxy isophotes), as a function of r_{eq} . The surface-brightness contours are presented in Fig. 15 superimposed to a g' GMOS image. The behaviour of all these parameters, which can be globally followed on Fig. 15, is a direct consequence of the complex structure of the galaxy. The ϵ decreases from a central value of ~ 0.4 down to ~ 0.05 while reaching 50 arcsec. This radial range corresponds to the elliptical isophotes of our inner component, i.e. a disc we will describe below. Further out, ϵ rises slightly but remaining smaller

than 0.1, and finally approaches 0 between 110 and 120 arcsec. The PA presents a clear variation from 132 to 92 deg that is a change of ~ 40 deg between 40 and 60 arcsec. The global behaviour of ϵ and PA agree with those presented by Goudfrooij et al. (1994) within their more limited radius of ~ 40 arcsec. Finally, the A4 coefficient confirms earlier statements that there are boxy isophotes ($A4 < 0$) in NGC 3610, as pointed out by Scorza & Bender (1990) for instance, which is considered as a clear evidence of past mergers. These boxy isophotes are present between ~ 20 (the lower limit of our fit) and ~ 45 arcsec and can also be identified in Fig. 15. At larger semi-axes, A4 is positive and varies continuously reaching a maximum at ~ 60 arcsec. Looking at the global picture, the behaviour of these parameters agree with the existence of a slope change in the light profile between ~ 50 and ~ 60 arcsec, where our inner component fades away, and the outer component dominates further out.

According to the characteristics of our inner component (Sérsic index $n \sim 0.8$ and $r_{\text{eff}} \sim 13$ arcsec), it corresponds to the inner disc already detected by Scorza & Bender (1990) in this galaxy, that we identify through the elliptical isophotes for $r_{\text{eq}} < 50$ arcsec, with a PA = 132 deg, which agrees perfectly with their PA. However, with our GMOS images, this inner disc can now be traced up to a much larger radius, ~ 60 arcsec. This disc is aligned with the small 3 arcsec twisted ‘inner disc’ detected by Whitmore et al. (1997), and they are probably a part of the same component whose central region shows a very steep rise in the surface-brightness profile, reaching $\mu_{g'0} \sim 19$ mag arcsec $^{-2}$. It is interesting to note that the extent we obtain for this disc agrees with the R_g where the GC density profile deviates from the power law (see Fig. 9) and with the radial range where the (inner) GC population is dominated by red clusters (see also Fig. 8), all likely related to the merger event.

As said above, our GMOS images let us reach further out than previous studies and fully characterize the outer component. In spite of the low surface brightness of the outer region, we are able to recover a Sérsic model with a shape index $n \sim 1.1$ and a quite large $r_{\text{eff}} \sim 47$ arcsec, i.e. a bulge-/spheroidal-extended component associated with the fine-structure present in the surface-brightness distribution. According to the light profile (Fig. 13), it extends up to a minimum $R_g \sim 180$ arcsec where the limiting surface brightness of 28 mag arcsec $^{-2}$ is reached in the g' band. It corresponds to the ‘bulge’ modelled by Scorza & Bender (1990) up to a much shorter $R_g \sim 100$ arcsec. Searching for a correlation between the stellar and GC populations, it is worth noting that the GC candidates located between 1 and 2 arcmin (Fig. 7) present the usual bimodal colour distribution, while further out, a small subsample of clusters between 2 and 4 arcmin mainly show up at an ‘intermediate’ colour range [mean $(g' - i')_0 = 0.87$].

In order to draw a picture of the galaxy’s outer structure, we obtained a residual map by subtracting from the original g' -band image a smoothed galaxy model performed with ELLIPSE and BMODEL within IRAF, where the central region has been masked in order to enhance the external features. The resulting image is presented in the left-hand panel of Fig. 16, where a complex underlying structure can be seen with unprecedented detail, including a wealth of shells and faint plumes, indicated with arrows, and a global X-structure. They appear over the whole GMOS image, covering the FOV of 5.5×5.5 arcmin 2 , that is, taking into account that we are just looking at a projected brightness distribution, they seem to be mostly associated with the outer spheroidal component quoted above. They are clearly indicating a recent history of strong tidal interactions and perturbations.

The $(g' - i')$ colour map depicted on the right-hand panel of Fig. 16 shows that there is no axisymmetric distribution, but a

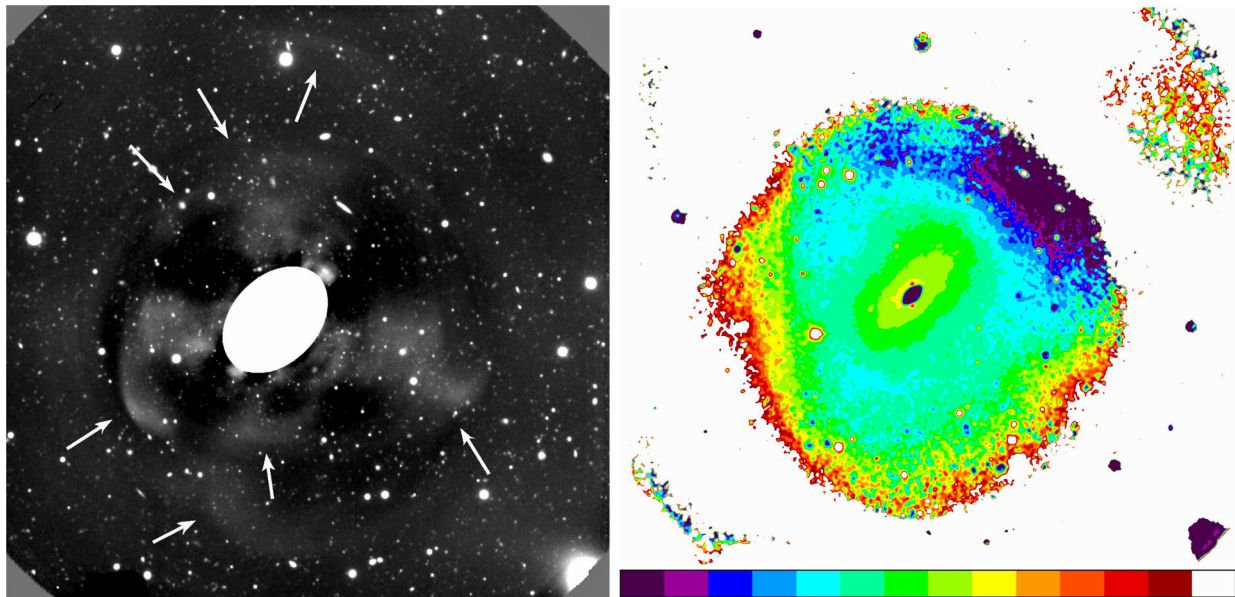


Figure 16. Left: GMOS image of NGC 3610 (N3610F) in the g' band, once the smoothed component of the galaxy is subtracted. White arrows indicate shells and plumes. Right: smoothed $(g' - i')$ colour map of the NGC 3610. The colour bar shown at the bottom spans from $(g' - i') = 0.8$ to 1.5

large-scale mild colour gradient is present in the global stellar population. It spans from blue [$(g' - i') \sim 0.8$] at the NW to red [$(g' - i') \sim 1.5$] towards the opposite SE side, following a similar direction as the semimajor axes of the inner galaxy (disc) isophotes. No traces of dust can be detected in the galaxy body, but the lack of a global radially symmetric colour distribution is understood as another piece of evidence of a past merger.

5 DISCUSSION

It is quite clear that NGC 3610 is a dynamically young, merger remnant, as shown by the plenty of features in the surface-brightness distribution, the inner embedded disc (within an elliptical galaxy), the boxy isophotes, the presence of spectroscopically confirmed young and metal-rich clusters, etc. To this picture, we add a new determination of the extent of that inner disc and of the spheroidal outer component, much larger than previously stated, a new image of the large-scale fine-structure with a detail never achieved before, and a colour map with a visible gradient. With respect to the GCs, we also obtained the extent of the whole system in NGC 3610, i.e. 40 kpc (Section 3.3), and analysed them up to this new R_g . The new analysis of the GC subpopulation for $R_g > 1$ arcmin includes a GC bimodal colour distribution between $1 < R_g < 2$ arcmin and the presence of a small subsample of clusters with ‘intermediate’ colours [mean $(g' - i')_0 = 0.87$] hosted by the outer component ($2 < R_g < 4$ arcmin).

In order to gather more information about these outer objects of intermediate colours, that seem to be present at $R_g < 1$ arcmin too, we can compare their mean colour with theoretical models of SSPs, as we have already done for NGC 1316 and NGC 4753 (Richtler et al. 2012; Caso et al. 2015), which presented similar intermediate-colour cluster subpopulations. Considering the models performed by Bressan et al. (2012), assuming SSPs with abundances $0.5-1 Z_\odot$, a Chabrier (2001) lognormal IMF, and absorption $A_V = 0.03$ (NED), the mean colour of these clusters corresponds to a population of 1.5–3 Gyr. These values are consistent with the ages and metallicities obtained by Strader et al. (2003, 2004) for the spectroscopically confirmed young clusters W6 and W11, though they

are located much closer to the galaxy, at $R_g = 22.7$ and 13.7 arcsec, respectively (Strader et al. 2004). At first, we cannot exclude the idea that the outer cluster subpopulation of NGC 3610, with intermediate colours, may be older and more metal-poor objects. However, all the observational evidence points to NGC 3610 being an ‘intermediate-age’ merger remnant as, for instance, all the fine-structures present in the surface-brightness distribution as well as the colour gradient detectable in the galaxy stellar population, would have disappeared if the merger were much older. With this idea in mind, we can speculate whether the subpopulation of clusters with intermediate colours is associate to an intense burst (or series of bursts) of stars and cluster formation, that were triggered by a recent major merger of two gas-rich discs. Such major merger has already been proposed by, among others, Strader et al. (2003) who also explained why it is not possible to consider the infall of a minor galaxy as the origin of NGC 3610.

A different paradigm has been supported by Scorza & Bender (1995), who studied a sample of ‘discy ellipticals’, including NGC 3610 and proposed that the embedded stellar discs are not likely the result of an accretion or merger event, but are primordial. However, through their data and models they could not prove that this interpretation was unique (e.g. de Jong et al. 2004). Another discy elliptical integrating that sample was NGC 4660, which has a strong disc. Kemp et al. (2016) have recently reported that NGC 4660 has a long tidal filament which implies that this galaxy has undergone a tidal interaction, probably a major merger, in the last few Gyr. Moreover, Kemp et al. show that the filament may correspond to a residual from star formation induced in the disc by the interaction, 1–2 Gyr ago. In a similar way, it is hard to explain the properties of NGC 3610 and its GCS described above, in the context of a primordial embedded disc. On the contrary, the fact that NGC 3610 belongs to a loose galaxy group may have provided the suitable conditions for a major merger to take place.

Regarding the fine-structure, the presence of shells in galaxies is considered as an evidence of a recent merger, as the shells are stellar remnants of the pre-merger systems. Sikkema et al. (2006) studied the GCSs in a sample of six shell ellipticals, looking for relations between the merger and formation history of the GCs. They found

evidence of a GC population associated with a recent merger in two of them. Afterwards, Sikkema et al. (2007) focused on the study of the shell structures in these galaxies. They concluded that the shell distributions are better described by merger models, in detriment of tidal interactions (e.g. Thomson & Wright 1990) or asymmetric local star formation (e.g. Loewenstein, Fabian & Nulsen 1987).

6 SUMMARY AND CONCLUDING REMARKS

We investigated the dynamically young merger remnant NGC 3610 and its GCS. This massive galaxy is located in a low-density environment and has a quite rich fine-structure. Thanks to the large area covered by our GMOS data, complemented with archival ACS data from the innermost regions, we are able to study both the GCS and the galaxy, in their whole extent. Our main results are as follows:

(i) The GC colour distribution obtained from GMOS data can be separated in three radial ranges: the inner one ($30 \text{ arcsec} < R_g < 1 \text{ arcmin}$) is dominated by red GCs in agreement with the results obtained from ACS data; the intermediate range ($1 < R_g < 2 \text{ arcmin}$) presents the typical bimodal GC distribution, i.e. old to metal-poor and metal-rich GCs that, for instance, are expected to have inhabited the pre-merger discs; and the outer region ($2 < R_g < 4 \text{ arcmin}$) has a small subpopulation of clusters, most of them have ‘intermediate’ colours, i.e. between those of the blue and red GCs detected in the intermediate radial range. According to SSP models, this outer subpopulation may correspond to younger clusters originated in the merger, 1–3 Gyr ago, and a bunch of them may be present at smaller radii too.

(ii) The extent of the whole GCS, assuming this limit as the galactocentric distance at which the background-corrected surface density is equal to 30 per cent of the background level, is calculated as 40 kpc. The red and blue GC radial profiles are fitted by power laws, being the red profile steeper than the blue one. The inner region, where the profile gets flatter and departs from a power-law, is better fitted with a Hubble model. The effect of GC erosion is a likely explanation to this latter behaviour.

(iii) By means of the GCLF, we calculate a poor old GC population of about 500 ± 110 members, that corresponds to a low specific frequency $S_N \sim 0.8$. Such low S_N is more frequent for spiral galaxies of similar brightness as NGC 3610 than for ellipticals, what can be understood as another hint pointing to a recent disc–disc merger.

(iv) We determine the effective radii of a sample of GC candidates located in the ACS field and the spectroscopically confirmed clusters from Strader et al. (2004). According to their sizes and/or brightness, the two confirmed young metal-rich clusters are in the limit between GCs and UCDs.

(v) From the analysis of the galaxy surface-brightness profile, we confirm the presence of an inner embedded disc and clear boxy isophotes. We perform new determinations of the extent of such inner disc (10 kpc) and the outer spheroidal component (30 kpc). We also obtain a residual map that shows the fine-structure with a degree of detail never achieved before. Finally, a colour gradient is detected on the galaxy colour map.

All our results support the interpretation of NGC 3610 as a recent merger remnant, probably a major disc–disc one, with a cluster population integrated by bona fide old GCs presumably born in the discs, as well as younger clusters originated in the merger, that can be detected at different radii. Moreover, we can speculate whether a two-pass merger may have occurred, with more gaseous dissipation on the first pass that deposited slightly older (redder) clusters nearer the centre, and a second pass that originated the

clusters with ‘intermediate’ colours in the outer region. We expect to study spectroscopically these few ‘intermediate’ colour clusters found in the outskirts, in the near future.

ACKNOWLEDGEMENTS

We appreciated the insightful and constructive comments of the referee, which improved this paper. This work was funded with grants from Consejo Nacional de Investigaciones Científicas y Técnicas de la República Argentina (PIP 112-201101-00393), Agencia Nacional de Promoción Científica y Tecnológica (PICT-2013-0317) and Universidad Nacional de La Plata (UNLP 11-G124), Argentina.

This work is based on observations obtained at the Gemini Observatory (GN2013A-Q-42), which is operated by the Association of Universities for Research in Astronomy, Inc., under a cooperative agreement with the NSF on behalf of the Gemini partnership: the National Science Foundation (United States), the National Research Council (Canada), CONICYT (Chile), the Australian Research Council (Australia), Ministério da Ciência, Tecnologia e Inovação (Brazil) and Ministerio de Ciencia, Tecnología e Innovación Productiva (Argentina). This work is also based on observations made with the NASA/ESA *Hubble Space Telescope*, obtained from the data archive at the Space Telescope Science Institute. STScI is operated by the Association of Universities for Research in Astronomy, Inc. under NASA contract NAS 5-26555. This research has made use of the NASA/IPAC Extragalactic Database (NED) which is operated by the Jet Propulsion Laboratory, California Institute of Technology, under contract with the National Aeronautics and Space Administration.

REFERENCES

- Barnes J. E., Hernquist L., 1992, *ARA&A*, 30, 705
 Bassino L. P., Faifer F. R., Forte J. C., Dirsch B., Richtler T., Geisler D., Schubert Y., 2006, *A&A*, 451, 789
 Bassino L. P., Richtler T., Dirsch B., 2008, *MNRAS*, 386, 1145
 Bertin E., Arnouts S., 1996, *A&AS*, 117, 393
 Binney J., Tremaine S., 1987, *Galactic Dynamics*. Princeton Univ. Press, Princeton, NJ
 Blakeslee J. P., Lucey J. R., Barris B. J., Hudson M. J., Tonry J. L., 2001, *MNRAS*, 327, 1004
 Bressan A., Marigo P., Girardi L., Salasnich B., Dal Cero C., Rubele S., Nanni A., 2012, *MNRAS*, 427, 127
 Brockamp M., Küpper A. H. W., Thies I., Baumgardt H., Kroupa P., 2014, *MNRAS*, 441, 150
 Brodie J. P., Romanowsky A. J., Strader J., Forbes D. A., 2011, *AJ*, 142, 199
 Brüns R. C., Kroupa P., 2012, *A&A*, 547, A65
 Cantiello M., Blakeslee J., Raimondo G., Brocato E., Capaccioli M., 2007, *ApJ*, 668, 130
 Cappellari M. et al., 2011, *MNRAS*, 413, 813
 Caso J. P., Bassino L. P., Richtler T., Smith Castelli A. V., Faifer F. R., 2013a, *MNRAS*, 430, 1088
 Caso J. P., Richtler T., Bassino L. P., Salinas R., Lane R. R., Romanowsky A., 2013b, *A&A*, 555, A56
 Caso J. P., Bassino L. P., Richtler T., Calderón J. P., Smith Castelli A. V., 2014, *MNRAS*, 442, 891
 Caso J. P., Bassino L. P., Gómez M., 2015, *MNRAS*, 453, 4421
 Chabrier G., 2001, *ApJ*, 554, 1274
 Chiboucas K. et al., 2011, *ApJ*, 737, 86
 Ciotti L., 1991, *A&A*, 249, 99
 de Jong R. S., Simard L., Davies R. L., Saglia R. P., Burstein D., Colless M., McMahan R., Wegner G., 2004, *MNRAS*, 355, 1155
 de Vaucouleurs G., de Vaucouleurs A., Corwin H. G., Jr, Buta R. J., Paturel G., Fouqué P., 1991, *Third Reference Catalogue of Bright Galaxies*.

- Volume I: Explanations and references. Volume II: Data for galaxies between 0^h and 12^h . Volume III: Data for galaxies between 12^h and 24^h . Springer-Verlag, New York, NY
- Denicoló G., Terlevich R., Terlevich E., Forbes D. A., Terlevich A., 2005, *MNRAS*, 358, 813
- Dirsch B., Richtler T., Geisler D., Forte J. C., Bassino L. P., Gieren W. P., 2003, *AJ*, 125, 1908
- Ebner K., Davis M., Djorgovski S., 1988, *AJ*, 95, 422
- Escudero C. G., Faifer F. R., Bassino L. P., Calderón J. P., Caso J. P., 2015, *MNRAS*, 449, 612
- Faifer F. R. et al., 2011, *MNRAS*, 416, 155
- Fall S. M., Zhang Q., 2001, *ApJ*, 561, 751
- Forbes D. A., Pota V., Usher C., Strader J., Romanowsky A. J., Brodie J. P., Arnold J. A., Spitler L. R., 2013, *MNRAS*, 435, L6
- Fouque P., Gourgoulhon E., Chamaraux P., Paturel G., 1992, *A&AS*, 93, 211
- García A. M., 1993, *A&AS*, 100, 47
- Georgiev I. Y., Goudfrooij P., Puzia T. H., 2012, *MNRAS*, 420, 1317
- Goudfrooij P., Hansen L., Jorgensen H. E., Norgaard-Nielsen H. U., de Jong T., van den Hoek L. B., 1994, *A&AS*, 104
- Goudfrooij P., Gilmore D., Whitmore B. C., Schweizer F., 2004, *ApJ*, 613, L121
- Goudfrooij P., Schweizer F., Gilmore D., Whitmore B. C., 2007, *AJ*, 133, 2737
- Harris W. E., 2009, *ApJ*, 699, 254
- Harris W. E., van den Bergh S., 1981, *AJ*, 86, 1627
- Harris W. E., Harris G. L. H., Alessi M., 2013, *ApJ*, 772, 82
- Hernquist L., Spergel D. N., 1992, *ApJ*, 399, L117
- Howell J. H., Brodie J. P., Strader J., Forbes D. A., Proctor R., 2004, *AJ*, 128, 2749
- Jordán A. et al., 2004, *ApJS*, 154, 509
- Jordán A. et al., 2005, *ApJ*, 634, 1002
- Jordán A. et al., 2007, *ApJS*, 171, 101
- Kemp S. N. et al., 2016, *ApJ*, 830, 66
- King I., 1962, *AJ*, 67, 471
- King I. R., 1966, *AJ*, 71, 64
- Kruijssen J. M. D., 2014, *Class. Quantum Gravity*, 31, 244006
- Kruijssen J. M. D., 2015, *MNRAS*, 454, 1658
- Kruijssen J. M. D., Pelupessy F. I., Lamers H. J. G. L. M., Portegies Zwart S. F., Bastian N., Icke V., 2012, *MNRAS*, 421, 1927
- Lane R. R., Salinas R., Richtler T., 2013, *A&A*, 549, A148
- Larsen S. S., 1999, *A&AS*, 139, 393
- Liu J., 2011, *ApJS*, 192, 10
- Loewenstein M., Fabian A. C., Nulsen P. E. J., 1987, *MNRAS*, 229, 129
- Madore B. F., Freedman W. L., Bothun G. D., 2004, *ApJ*, 607, 810
- Masters K. L. et al., 2010, *ApJ*, 715, 1419
- Michard R., Marchal J., 1994, *A&AS*, 105
- Mieske S., Hilker M., Infante L., 2004, *A&A*, 418, 445
- Misgeld I., Mieske S., Hilker M., Richtler T., Georgiev I. Y., Schuberth Y., 2011, *A&A*, 531, A4
- Muratov A. L., Gnedin O. Y., 2010, *ApJ*, 718, 1266
- Norris M. A. et al., 2014, *MNRAS*, 443, 1151
- Puzia T. H., Paolillo M., Goudfrooij P., Maccarone T. J., Fabbiano G., Angelini L., 2014, *ApJ*, 786, 78
- Richtler T., 2003, in Alloin D., Gieren W., eds, *Lecture Notes in Physics*, Vol. 635, *Stellar Candles for the Extragalactic Distance Scale*. Springer-Verlag, Berlin, p. 281
- Richtler T., Bassino L. P., Dirsch B., Kumar B., 2012, *A&A*, 543, A131
- Salinas R., Alabi A., Richtler T., Lane R. R., 2015, *A&A*, 577, A59
- Schlafly E. F., Finkbeiner D. P., 2011, *ApJ*, 737, 103
- Schweizer F., Seitzer P., 1992, *AJ*, 104, 1039
- Scorza C., Bender R., 1990, *A&A*, 235, 49
- Scorza C., Bender R., 1995, *A&A*, 293, 20
- Sérsic J. L., 1968, *Atlas de Galaxias Australes*. Observatorio Astronomico, Cordoba
- Sikkema G., Peletier R. F., Carter D., Valentijn E. A., Balcells M., 2006, *A&A*, 458, 53
- Sikkema G., Carter D., Peletier R. F., Balcells M., Del Burgo C., Valentijn E. A., 2007, *A&A*, 467, 1011
- Sirianni M. et al., 2005, *PASP*, 117, 1049
- Smith J. A. et al., 2002, *AJ*, 123, 2121
- Spitler L. R., Forbes D. A., Strader J., Brodie J. P., Gallagher J. S., 2008, *MNRAS*, 385, 361
- Stetson P. B., 1987, *PASP*, 99, 191
- Strader J., Brodie J. P., Huchra J. P., 2003, *MNRAS*, 339, 707
- Strader J., Brodie J. P., Forbes D. A., 2004, *AJ*, 127, 295
- Thomson R. C., Wright A. E., 1990, *MNRAS*, 247, 122
- Tonry J. L., Dressler A., Blakeslee J. P., Ajhar E. A., Fletcher A. B., Luppino G. A., Metzger M. R., Moore C. B., 2001, *ApJ*, 546, 681
- Tully R. B. et al., 2013, *AJ*, 146, 86
- Whitmore B. C., Miller B. W., Schweizer F., Fall S. M., 1997, *AJ*, 114, 1797
- Whitmore B. C., Schweizer F., Kundu A., Miller B. W., 2002, *AJ*, 124, 147
- Whitmore B. C., Chandar R., Bowers A. S., Larsen S., Lindsay K., Ansari A., Evans J., 2014, *AJ*, 147, 78

This paper has been typeset from a $\text{\TeX}/\text{\LaTeX}$ file prepared by the author.